Specialty Journal of Pharmacognosy, Phytochemistry, and Biotechnology
ISSN: 3062-441X
2022, Volume 2, Page No: 178-201

Available online at: www.galaxypub.co/page/journals

Galaxy Publication

Galaxy Publication

Understanding the Role and Prognostic Significance of Prostaglandin D2 Signaling in Lung Adenocarcinoma

Lucas Ferreira[1], André Cunha[1], Renato Lopes[1], Bruno Azevedo[1], Mariana Rocha[1]*

[1]Department of Pharmaceutical Biotechnology, Faculty of Pharmacy, Federal University of Rio Grande do Sul, Porto Alegre, Brazil.

***E-mail** ✉ mariana.rocha.pb@gmail.com

Received: 14 August 2022; **Revised:** 21 November 2022; **Accepted:** 23 November 2022

ABSTRACT

Although metabolic reprogramming is a defining feature of cancer, the ways in which metabolites mediate communication between cells remain largely unexplored. To bridge this knowledge gap, we investigated metabolite-driven intercellular interactions using single-cell RNA sequencing (scRNA-seq) data to delineate the metabolic architecture of the tumor microenvironment (TME) in lung adenocarcinoma (LUAD) and uncover novel metabolite signaling pathways. Dimensionality reduction of the scRNA-seq dataset was performed with the Seurat package, and cell types were manually annotated using canonical markers from Cell Marker 2.0 and prior studies. Metabolite abundance and potential cell–cell communication events were inferred with MEBOCOST. In parallel, immune infiltration levels and tumor activity scores in the TCGA-LUAD cohort were evaluated using ESTIMATE and ssGSEA algorithms, and survival analyses were conducted for genes implicated in identified signaling axes. Key findings were validated across two independent GEO datasets. The expression of PTGDS and PTGDR was further verified using RT-qPCR and fluorescence in situ hybridization. Five metabolites—prostaglandin D2 (PGD2), D-Mannose, Choline, L-Cysteine, and Cholesterol—were identified as prominent components of the LUAD TME. PGD2 was a central signaling metabolite, predominantly produced by fibroblasts and plasmacytoid dendritic cells via PTGDS, and by mast cells through HPGDS. PGD2 signaling primarily targeted NK/T cells expressing the receptor PTGDR, and endothelial cells mediated its transport via SLCO2A1. CX3CR1+ NK/T cells participated in autocrine PGD2 signaling, whereas KLRC2+ NK cells, DNAJB1+ NK cells, and CD8+ MAIT cells were engaged in paracrine interactions. PGD2 may additionally facilitate lactate export through SLCO2A1 on endothelial cells. Clinically, this signaling axis correlated with infiltration of cytotoxic immune cells such as DNAJB1+ NK cells and was associated with favorable prognosis. A risk model derived from this axis predicted patient response to immunotherapy across both immunologically "hot" and "cold" tumors, suggesting potential therapeutic options for low-risk patients. RT-qPCR and immunofluorescence further confirmed decreased expression of PTGDS and PTGDR in LUAD tumors compared with normal tissue. Overall, our findings highlight PGD2 and its associated signaling network as critical modulators of tumor-suppressive and anti-inflammatory processes in LUAD, providing promising avenues for prognosis assessment and therapeutic intervention.

Keywords: Prognostic model, Metabolic signaling, CX3CR1+ NK/t cells, Prostaglandin D2, Lung adenocarcinoma

How to Cite This Article: Ferreira L, Cunha A, Lopes R, Azevedo B, Rocha M. Understanding the Role and Prognostic Significance of Prostaglandin D2 Signaling in Lung Adenocarcinoma. Spec J Pharmacogn Phytochem Biotechnol. 2022;2:178-201. https://doi.org/10.51847/UKPC3YL5uI

Introduction

In recent decades, the alteration of tumor metabolism within the tumor microenvironment (TME) has emerged as a critical feature of cancer progression and a potential target for therapeutic intervention [1-3]. Beyond fueling tumor growth, metabolites serve as messengers, traveling between cells to modulate behavior and facilitate intercellular communication [1, 4, 5]. For example, in pancreatic cancer, cancer-associated fibroblasts (CAFs) supply cysteine through the TGF-β/SMAD3/ATF4 pathway, directly influencing tumor metabolism [6]. Despite

such insights, the full extent of how metabolites orchestrate cross-talk in the TME remains poorly understood, largely due to technical limitations. Recent computational tools that infer metabolic activity from single-cell transcriptomic data, including MEBOCOST, have opened new avenues for exploring these complex interactions [7-10].

Lung cancer is one of the most prevalent malignancies globally, representing roughly one-eighth of all cancer cases [11], with lung adenocarcinoma (LUAD) being its most common subtype [12]. Research on metabolic markers in LUAD is gaining momentum, although studies are often limited by small sample sizes and high variability [13-16]. A systematic review has associated over 150 metabolites with altered metabolic processes in lung cancer [17], yet clinical application remains challenging due to frequent false positives and incomplete mechanistic understanding. While LUAD prognosis has been extensively studied through histopathology, genomics, transcriptomics, proteomics, and microbiome analyses, there is still a lack of research focusing on metabolites and the signaling networks they mediate within the TME.

To address this gap, we analyzed a baseline LUAD single-cell RNA sequencing (scRNA-seq) dataset to quantify metabolite levels and predict intercellular communication events **(Figure 1a)**. Among the metabolites identified, prostaglandin D2 (PGD2) stood out as a central mediator in the TME, directing communication between various immune and stromal cells. We mapped the primary PGD2-producing cells and their recipient populations, uncovering its anti-tumor activity via activation of T cells and NK cells through the PGD2 receptor (PTGDR). The expression of these key genes was validated at both transcript and protein levels using retrospective patient samples. Additionally, the findings were confirmed across three bulk RNA-seq datasets, emphasizing the clinical relevance of the PGD2-associated metabolic signaling axis. Overall, this study highlights the role of PGD2 in LUAD and provides a framework for exploring metabolite-driven biomarkers as prognostic and therapeutic tools.

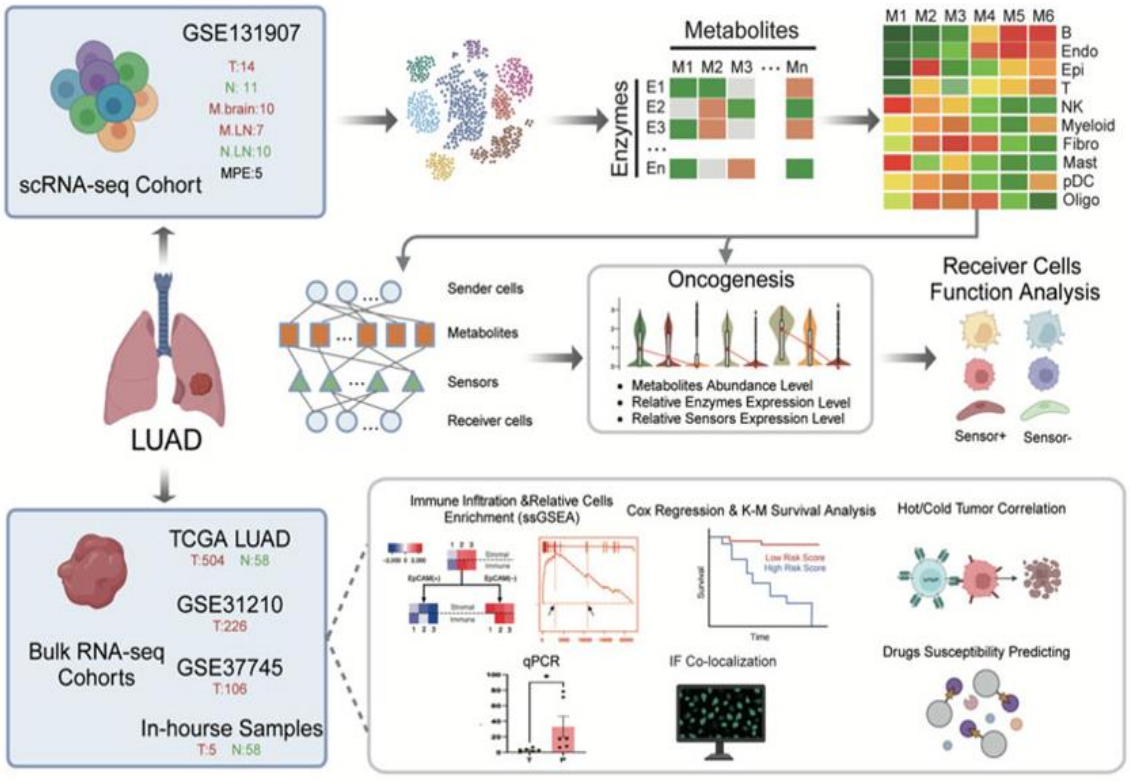

a)

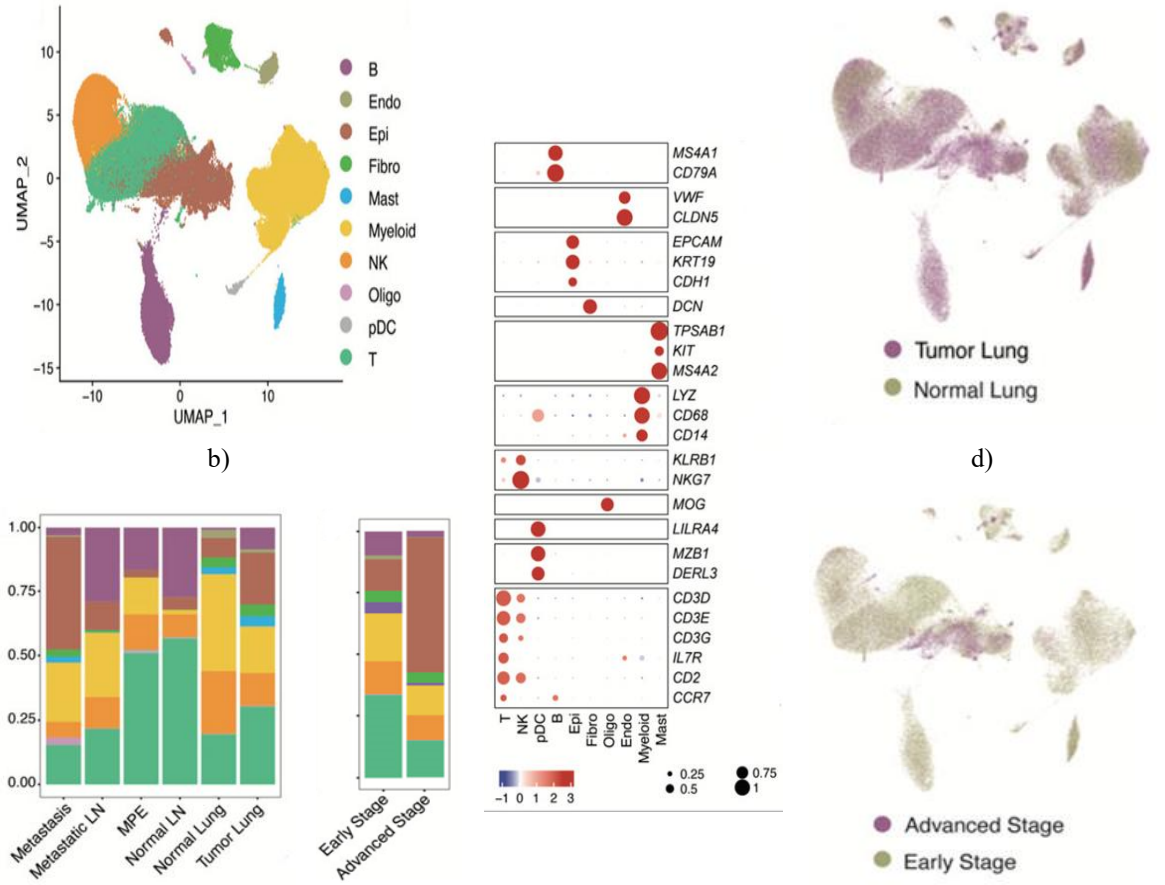

Figure 1. Schematic workflow diagram of this study and single-cell transcriptome atlas of LUAD. (a) The panel depicts the overall analytical workflow. (b) A UMAP visualization of 177,042 cells, grouped according to cell type. (c) A dot-based representation highlighting the expression patterns of canonical marker genes across principal cell populations. Color saturation corresponds to the Z-score–standardized mean expression, whereas dot size reflects the proportion of cells assigned to each cell type. (d) A UMAP view distinguishing cells originating from lung tumor and normal tissues. (e) Distribution of cell types across the sampled anatomical regions. (f) Comparison of cellular composition across disease stages, in which stage I–III samples are classified as early stage and stage IV as advanced stage. (g) UMAP visualization separating early-stage versus advanced-stage cells. Abbreviations: B: B cells; Endo: endothelial cells; Epi: epithelial cells; Fibro: fibroblasts; Mast: mast cells; Myeloid: myeloid populations excluding pDCs and Mast cells; NK: Natural Killer cells; Oligo: oligodendrocytes; pDC: plasmacytoid dendritic cells; T: T cells.

Materials and Methods

Data collection

The scRNA-seq dataset GSE131907 [18] was retrieved from the GEO database. Following preliminary filtering, the dataset contained 208,506 immune cells meeting basic quality standards. The cohort comprised 58 samples derived from 44 treatment-naïve LUAD patients, including 15 primary tumors, 11 distant normal lung regions, 10 normal lymph nodes, 10 metastatic brain lesions, and seven metastatic lymph nodes. Additionally, pleural fluid from five malignant pleural effusion cases was incorporated.

After deeper quality assessment, sample EBUS_49 (GSM3827138)—from an advanced-stage individual—was excluded due to excessive red blood cell contamination. Cells were subsequently removed if they met any of the following criteria:

- Reads Count < 500
- Feature Numbers < 200
- Mean UMI per gene < 0.8

- Mitochondrial gene percentage > 10%
- Ribosomal gene percentage > 60%

Doublets were identified with DoubletFinder (DoubletRatePer = 0.005) and eliminated. Ultimately, 185,197 high-quality cells remained for GSE131907 and were retained for downstream analyses.
For bulk transcriptomic validation, three external LUAD datasets were incorporated. The TCGA LUAD cohort contributed 562 TPM-normalized samples (504 tumor, 58 distant normal lung). Two GEO microarray datasets—GSE31210 (225 LUAD tumors) and GSE37745 (106 LUAD tumors)—were preprocessed by mapping probes to gene symbols using their respective platform annotations, averaging signals when multiple probes corresponded to the same gene.

Clustering and major cell type identification in scRNA-seq data
All single-cell analyses were performed with Seurat v5.1.0 [19]. Read counts were normalized using NormalizeData(LogNormalize). Cell cycle status was determined with CellCycleScoring, using 43 S-phase and 54 G2/M-phase markers to compute S.Score, G2M.Score, Phase, and CC.Difference (S.Score − G2M.Score).
Highly variable genes were selected via FindVariableFeatures (method = vst, nfeatures = 2000), excluding mitochondrial, hemoglobin, ribosomal, immunoglobulin, T-cell receptor genes, and AC233755.1. Data scaling (ScaleData) incorporated nCount_RNA, nFeature_RNA, and CC.Difference as regression variables.
Unsupervised dimensionality reduction was carried out using RunPCA (30 PCs). Batch effects among samples were corrected with RunHarmony (harmony v1.2.1). Neighbor graphs were constructed via FindNeighbors using harmony-corrected dimensions (n.neighbors = 40, min.dist = 0.5, dims = 1:30), followed by clustering with FindClusters at resolution 0.1.
Inspection of UMAP embeddings identified 8,155 cells clustering with epithelial cells yet expressing CD3D but lacking EPCAM; these were removed as contaminants. Reanalysis of the remaining cells yielded 177,042 final high-quality cells, forming the definitive clustering set.
Cluster identities were assigned through curated marker genes derived from the literature and the CellMarker 2.0 resource.

- Clusters 1 and 5 → Myeloid cells (LYZ, CD68, CD14).
- Cluster 3 → NK cells (KLRB1, NKG7).
- Cluster 4 → B cells (MS4A1, CD79A).
- Cluster 6 → Fibroblasts (DCN).
- Cluster 7 → Mast cells (TPSAB1, KIT, MS3A2).
- Cluster 8 → Endothelial cells (VWF, CLDN5).
- Cluster 9 → pDCs (MZB1, DERL3, LILRA4).
- Cluster 10 → Epithelial cells (EPCAM, KRT19, CDH1).
- Cluster 11 → Oligodendrocytes (MOG).
- Clusters 0, 12, 13, 14 → T cells (CD3D, CD3E, CD3G, IL7R, CD2, CCR7).

Metabolic cell–cell communication analysis by MEBOCOST
To quantify metabolite-mediated communication stress, large cell categories (>6,000 cells) were randomly downsampled to 6,000 cells per type, forming the input metabolite estimation matrix. Metabolic communication was inferred using MEBOCOST v1.0.4 [10]. Parameters included:

- cutoff_exp = 0
- cutoff_met = 0
- cutoff_prop = 0.01 (≥1% of cells expressing a metabolite or sensor)

Permutation-based FDR assessment (permutation_test_fdr) retained metabolite–sensor interactions with pval_cutoff = 0.9.
To compare metabolite abundance among cell groups, the inferred metabolite matrix was formatted into a Seurat object. The top 200 variable features were selected, followed by PCA, FindNeighbors, and FindClusters using parameters aligned with the original scRNA-seq clustering workflow.
Visualization of communication scores used custom thresholds:

- pval_cutoff = 0.01

- comm_score_cutoff = 1
- cutoff_prop = 0.1 for both sender and receiver categories

Key metabolites per cell type were determined using the criteria:

- log2FoldChange > 0
- p.adjust < 0.001 (Wilcoxon test)
- comm_score > 1

Because some metabolites lacked annotated sensors, only metabolites exhibiting detectable communication patterns were labeled in **Figure 2c**.

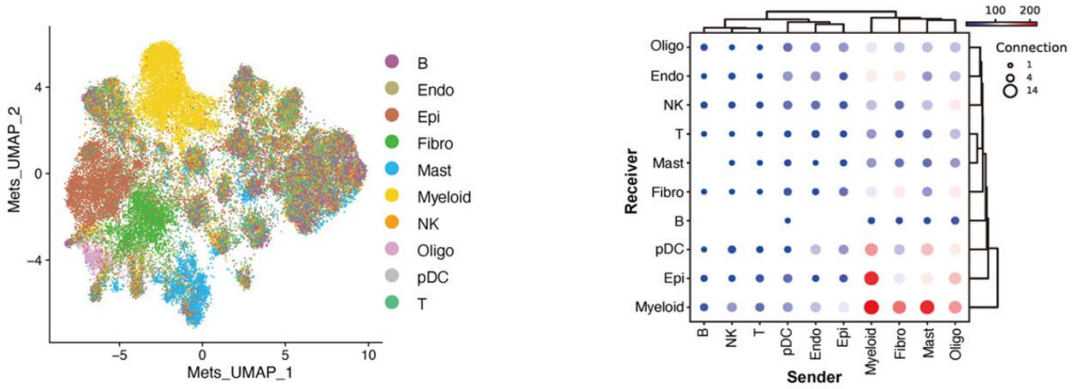

a) b)

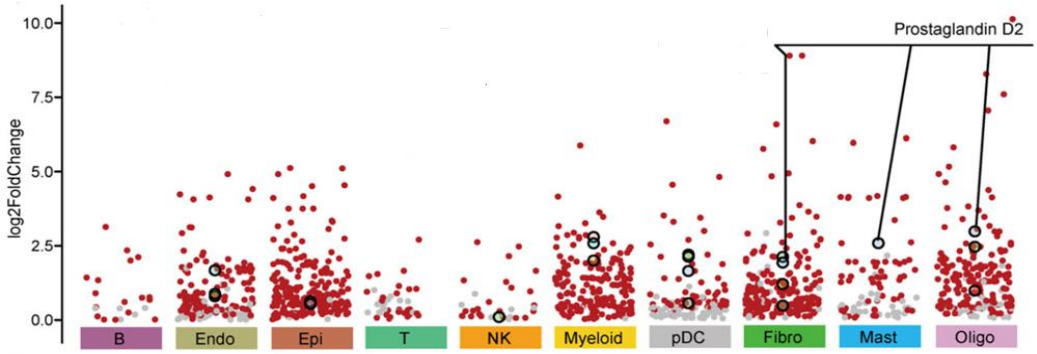

c)

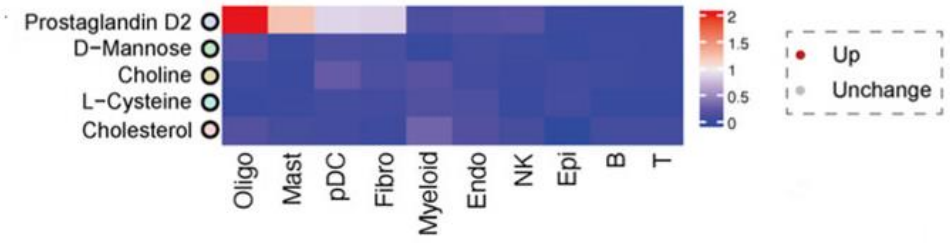

d)

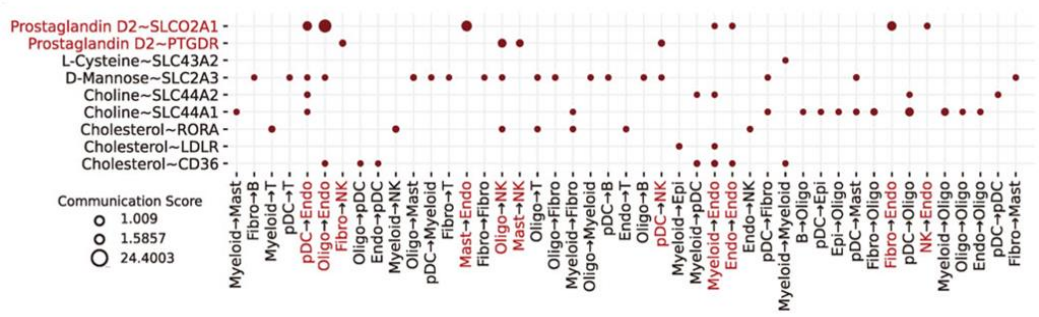

e)

Figure 2. Estimation of metabolites and their differential abundance with sensor expression across cell types. (a) A UMAP representation constructed from the 200 most variable metabolite-associated features is shown, with cells annotated by their corresponding cell type. (b) A pairwise interaction map visualizes metabolite-sensor communication between distinct cellular populations. Sender cell types are displayed on the x-axis and receiver types on the y-axis. Dot magnitude reflects the number of metabolite-sensor signaling events detected between each pair, while dot coloration indicates the overall confidence score for those interactions. Only communication events fulfilling the criteria of metabolite communication score >1 and metabolite/sensor detection proportions >0.1 in both sender and receiver are included. (c) Volcano plots illustrate metabolites exhibiting increased abundance (log2FoldChange >0) across 10 major cell types. Metabolites achieving Wilcoxon test p.adjust <0.001 are highlighted in red. The twenty metabolites with the most pronounced fold-change in each cell type—restricted to those also represented in panel (B)—are emphasized with enlarged, uniquely colored markers. (d) A heatmap presents the mean levels of the top differentially enriched metabolites across cell populations. (e) A detailed dot plot depicts the metabolite-sensor signaling events associated with the differential metabolites Prostaglandin D2, L-Cysteine, D-Mannose, Choline, and Cholesterol. Rows denote metabolite-sensor combinations, while columns correspond to sender cell types. Prostaglandin D2 is marked in red.

Re-clustering of NK and T cells

A total of 24,489 NK cells and 56,674 T cells were isolated and reanalyzed using the workflow applied in earlier scRNA-seq clustering. VariableFeatures (nfeatures = 2000) were identified, followed by scaling, PCA (30 components), and clustering steps identical to prior analyses.

For NK cell clustering, 30 PCs were used with a resolution of 0.4 and min.dist = 0.3. An initial removal of 6,146 EPCAM-positive but CD3D-negative cells was performed to eliminate contamination. The remaining 50,528 cells were reclustered using 15 PCs, again with resolution = 0.4 and min.dist = 0.3.

Thirteen NK clusters were annotated by integrating PTGDR and PTGDS expression patterns and previously established lineage markers [20]. Cluster one corresponded to CX3CR1+ NK cells. Cluster eight comprised DNAJB1+ NK cells. Clusters 0, 5, 7, 10, and 11 were assigned to KLRC2+ NK subsets. Clusters 2, 3, and six were grouped as RGS1+ NK cells. Due to the absence of robust defining markers, cluster nine was named Unknown NK1; clusters 4 and 13 as Unknown NK2; and cluster 12 as Unknown NK3.

T-cell annotation relied on CD8A and CD4 expression, revealing two dominant subsets. CD8+ T cells were further parsed into three populations:

- CD8+ T1, characterized by MAIT-associated genes (SLC4A10, ZBTB16, NCR3, RORA, KLRB1);
- CD8+ T2, displaying naïve T-cell markers (CCR7, SELL, TCF7, LEF1);
- CD8+ T3, enriched for cytotoxicity-related markers (GZMH, GNLY, GZMK, NKG7, GZMA).

Additional genes identified in recent literature—including KIR2DL4, CX3CR1, TYROBP, CXCR5, CD69, RPS12, CD52, NME1—were incorporated to refine CD8+ T-cell characterization [21].

All feature-density visualizations were produced with the plot_density function from Nebulosa v1.14.0 [22].

Validation expression of genes in PGD2 signaling axis

To corroborate expression patterns of PGD2 signaling components, several large-scale pan-cancer integrated single-cell datasets were employed. These datasets compile information across multiple cancers and encompass

fibroblast [23], myeloid [24], NK [20], and T-cell [21] lineages. Only data originating from LUAD or normal lung were extracted.
The fibroblast atlas (http://pan-fib.cancer-pku.cn) enabled evaluation of PTGDS expression, identifying its dominant fibroblast subpopulations and regional distribution.
Myeloid data from http://panmyeloid.cancer-pku.cn were used to map PTGDS and HPGDS expression in pDCs, mast cells, and broader myeloid subsets.
The NK cell dataset facilitated assessment of PTGDS and PTGDR in NK-mediated PGD2 sensing.
The T-cell atlas (http://cancer-pku.cn:3838/PanC_T) provided expression resolution for PTGDS and PTGDR specifically within CD8+ T-cell subsets.
Collectively, these resources supported systematic cross-validation of PGD2 pathway gene expression patterns across diverse cellular and tissue contexts.

Definition of gene sets for signature calculation
Functional comparison of SLCO2A1+/− Endo cells, PTGDS+/− NK cells, PTGDR+/− NK cells, and PTGDR+/− T cells utilized curated gene sets representing L-lactate dehydrogenase activity, cytotoxicity, inflammation, and cellular stress [20].

- L-lactate dehydrogenase gene set: LDHA, LDHB
- Cytotoxic gene set: GZMA, GZMB, GZMH, GZMM, GZMK, GNLY, PRF1, CTSW
- Inflammatory gene set: CCL2, CCL3, CCL4, CCL5, CXCL10, CXCL9, IL1B, IL6, IL7, IL15, IL18
- Stress-response gene set: BAG3, CALU, DNAJB1, DUSP1, EGR1, FOS, FOSB, HIF1A, HSP90AA1, HSP90AB1, HSP90B1, HSPA1A, HSPA1B, HSPA6, HSPB1, HSPH1, IER2, JUN, JUNB, NFKBIA, NFKBIZ, RGS2, SLC2A3, SOCS3, UBC, ZFAND2A, ZFP36, ZFP36L1

Scores for these gene sets were computed using AUCell.
A previously reported “hot tumor” score [25]—designed to quantify tumor immunologic activity—consisted of CCL19, CCR2, CCR4, CCR5, CD27, CD40LG, CD8A, CXCL10, CXCL11, CXCL13, CXCL9, CXCR3, CXCR6, FASLG, FGL2, GZMA, GZMH, IDO1, IFNG, IRF8, LAG3, LYZ, MS4A1, PDCD1, TBX21, TLR7, TLR8. This signature was calculated via ssGSEA in the bulk transcriptomic datasets.
Marker identification for the eight major cell lineages, along with the refined NK and T subpopulations, was performed using Seurat’s FindMarkers function, selecting the top twenty markers with $p < 0.05$ for each population.

Calculation of signature score
For the scRNA-seq analyses, signature scoring for each predefined gene set was performed using AUCell v1.26.0 [26]. Ranked gene–expression matrices were first generated through the AUCell_buildRankings function. These rankings were then used as input for AUCell_calcAUC, which produced the AUC-based signature scores. All gene sets referenced in this work correspond to those specified in the preceding sections.
To evaluate feature gene expression across major cellular populations, we additionally applied single-sample gene set enrichment analysis (ssGSEA) using GSVA v1.52.3 [27]. The gsva function was run with the settings method = "ssgsea", mx.diff = TRUE, and kcdf = "Gaussian". ssGSEA scores were subsequently used to infer the relative abundance of cell subsets in tumor microenvironment samples obtained from bulk RNA-seq and microarray datasets.
An additional metric—the Hot score—derived from the previously defined 27-gene signature, was calculated to characterize the immune activity of tumors. Samples with Hot score > 0 were interpreted as hot tumors, whereas those with Hot score < 0 were categorized as cold tumors.

Survival analysis
Survival-related statistical procedures were implemented using the survival v3.7.0 [28] and survminer v0.5.0 [29] R packages. Univariate and multivariate Cox regression models were constructed with coxph, providing regression coefficients, hazard ratios (HR), and corresponding p-values. After establishing the gene-based prognostic model, potential multicollinearity among the genes was examined using vif from the car package to guarantee independence among predictors.

Visualization of the Cox model results was performed using forestplot. To determine the optimal stratification point for survival comparison, the surv_cutpoint function was applied. Model fitting and the computation of log-rank p-values were carried out with survfit, and Kaplan–Meier survival curves were plotted using ggsurvplot. Predictive accuracy of the risk score was further quantified through time-dependent ROC analysis using survivalROC v1.0.3.1 [30] at 1-year (365 days), 3-year (1,095 days), and 5-year (1,828 days) endpoints.

Therapeutic response prediction

To estimate the half maximal inhibitory concentrations (IC50) for commonly administered antitumor drugs in LUAD, we employed the calcPhenotype function in the oncoPredict v1.2 package [31]. Training was performed on the integrated GDSC2Data resource, which encompasses 198 compounds and 805 cell line profiles. All parameters remained at their default configurations.

Clinical tissue collection

LUAD specimens were collected from patients diagnosed at Fuyang People's Hospital. Individuals with a prior history of malignancies or who had received neoadjuvant or preoperative therapy were excluded. Each patient contributed paired samples consisting of tumor tissue and distant, histologically normal lung tissue. Written informed consent was obtained from all participants before specimen acquisition.

RT-qPCR

Total RNA was isolated from tissue samples that had been pulverized under liquid-nitrogen conditions using TRIzol reagent (TaKaRa RNAiso Reagent 9180). The homogenates were incubated with TRIzol for 5 minutes at room temperature, after which chloroform (200 μL) was added. Phase separation was achieved by centrifugation at 12,000 × g for 15 minutes, and RNA was precipitated from the aqueous fraction using an equal volume of isopropanol. After washing with 75% ethanol, pellets were dissolved in RNase-free water (20 μL). RNA concentration and purity were assessed using a NanoDrop 2000 and 1.5% agarose gel electrophoresis.

cDNA synthesis was carried out using the PrimeScript™ RT Reagent Kit with gDNA Eraser (TaKaRa, RR047A). Genomic DNA was removed at 42°C for 2 minutes, followed by reverse transcription at 37°C for 15 minutes, and the reaction was terminated at 85°C for 5 seconds.

Quantitative PCR was conducted on a Bio-Rad CFX96 system using TB Green Premix Ex Taq™ (TaKaRa, RR420A). Reactions (20 μL total volume) contained:

- 10 μL TB Green Premix Ex Taq II
- 0.4 μL forward primer (10 μmol/L)
- 0.4 μL reverse primer (10 μmol/L)
- 1 μL cDNA template
- 8.2 μL RNase-free water

β-actin served as the internal control. The thermal cycling conditions were:

1. 95°C for 30 s
2. 45 cycles of:
    - 95°C for 5 s
    - 60°C for 30 s
3. Melting-curve analysis

Relative gene expression was computed using the 2^(−ΔΔCt) method, and results were presented as mean ± standard deviation.

Multiplex immunofluorescence staining

Multiplex immunofluorescence staining was carried out using the following procedure. Paraffin-embedded tissue sections were passed sequentially through xylene I (12 min), xylene II (12 min), absolute ethanol (6 min), 95% ethanol (6 min), and 85% ethanol (6 min), followed by rinsing in distilled water to accomplish dewaxing and rehydration. Antigen retrieval was then performed by immersing the slides in EDTA buffer (pH 8.0) and subjecting them to microwave treatment (8 min at medium heat, 8 min pause, and an additional 7 min at medium-low heat), after which they were allowed to cool at room temperature. Sections were washed three times in PBS (pH 7.4) for 5 min each.

Endogenous peroxidase activity was quenched using 3% hydrogen peroxide for 25 min at room temperature, followed by PBS washes. The slides were then incubated with 3% BSA for at least 30 min to block nonspecific binding. A primary antibody against CD8 (1:50 dilution) was applied, and the tissues were incubated overnight at 4°C. After PBS washing, a fluorescently conjugated secondary antibody (haokebio, HKI0029, Alexa Fluor 488) was applied for 50 min at room temperature in the dark. A brief incubation (3–5 min) with Flare signal amplification reagent was then used to enhance fluorescence intensity, followed by PBS washing.
The same staining cycle—from antigen retrieval onward—was repeated for the second primary antibody, which was detected using the Alexa Fluor 594–labeled secondary antibody (haokebio, HKI0029). Nuclear counterstaining was performed with DAPI for 8 min in the dark. After final PBS washes, sections were mounted using an anti-fade reagent. The primary antibodies used in this study included PTGDR (sanjingbio, Sj-AB11585), PTGDS (sanjingbio, Sj-AB16367), α-SMA (haokebio, HKA50033), CD56 (haokebio, 14255-AP), and CD8 (haokebio, I10361A).

Statistical analysis
All statistical evaluations were carried out in R v4.1.1. Depending on the comparison described in the figure legends, either the Wilcoxon rank-sum test or Student's t-test was selected. Pearson correlation coefficients were calculated to determine associations between PTGDR and PTGDS expression in NK cells, whereas Spearman correlation was used for non-parametric relationships shown in the heatmap. To discriminate hot versus cold tumors using gene expression and the risk score model, ROC curves were generated via the plotROC v2.3.1 package, and the AUC values were used to quantify classification performance.

Results and Discussion

Overall metabolic landscape of cells in LUAD
To characterize the metabolic and cellular heterogeneity of LUAD and its related tissues, we analyzed tumor lung (T: 14 samples), adjacent normal lung (N: 11), metastatic brain tissue (M.brain: 10), metastatic lymph node (M.LN: 7), normal lymph node (N.LN: 10), and malignant pleural effusion samples (MPE: 5) from the scRNA-seq dataset GSE131907 [18], which contains material from 44 untreated LUAD patients undergoing bronchoscopy or surgery. After removing low-quality cells and potential doublets, 177,042 high-quality single-cell transcriptomes remained.
Following normalization for read depth, gene counts, and Cell Cycle scores (see Methods), PCA was conducted on the top 2,000 highly variable genes. Batch effects were minimized using Harmony [32], generating well-integrated data without sample- or cell-cycle-driven separation. Harmony-corrected PCs were used to build a unified UMAP, followed by graph-based clustering and annotation using canonical marker genes. Ten primary cell populations were identified **(Figure 1b)**: epithelial cells (Epi; n = 26,144), T cells (n = 56,674), B cells (n = 21,903), fibroblasts (n = 4,430), plasmacytoid dendritic cells (pDC; n = 861), NK cells (n = 24,489), myeloid cells excluding pDC and mast cells (n = 36,294), endothelial cells (n = 2,107), and oligodendrocytes (n = 655) originating from brain metastasis samples. Marker expression for these groups is shown in **Figure 1c**. Tissue- and stage-related variation in cellular infiltration was evident **(Figures 1d–1g)**; tumor and metastatic tissues with dense epithelial content exhibited reduced immune infiltration, particularly NK cells, and this pattern intensified from early to late disease stages.
To examine metabolic patterns, subsets of major cell classes were downsampled to 6,000 cells each for metabolite estimation using MEBOCOST [10]. A total of 560 secreted metabolites detected in ≥1% of cells in at least one cell population were retained. PCA of the top 200 variable metabolites was performed, followed by UMAP embedding and clustering **(Figure 2a)**. Lymphoid cells showed metabolite profiles distinct from Myeloid, Epi, Fibro, Mast, pDC, and Oligo cells. All detectable metabolites, metabolic sensors, and corresponding signaling axes across 10 cell types were catalogued.
Analysis of metabolic communication patterns indicated that Myeloid, Fibro, Mast, and Oligo cells predominantly function as ligand-producing populations interacting with Endo, NK, Fibro, pDC, Epi, and Myeloid cells **(Figure 2b)**. Cell type–specific metabolites were ranked, and the top 20 involved in communication were used to identify hallmark metabolites, highlighting five key molecules—prostaglandin D2 (PGD2), D-Mannose, Choline, L-Cysteine, and Cholesterol **(Figures 2c and 2d**). The corresponding metabolic-receptor signaling axes included prostaglandin D2 ~ SLCO2A1, prostaglandin D2 ~ PTGDR, L-Cysteine ~ SLC43A2, D-Mannose ~ SLC2A3,

Choline ~ SLC44A2/SLC44A1, and Cholesterol ~ RORA/LDLR/CD36 **(Figure 2e)**. Choline, L-Cysteine, and Cholesterol are well-established players in cancer biology [33-35].

Of particular note, PGD2 displayed the highest abundance in Mast, Oligo, Fibro, and pDC cells—immune or stromal subsets rarely emphasized in LUAD research **(Figure 2d)**. Its signaling axes suggest meaningful metabolic involvement: PGD2 ~ SLCO2A1 interactions were primarily directed toward Endo cells, whereas PGD2 ~ PTGDR signaling linked stromal or myeloid sources to NK cells **(Figure 2e).**

Tumor-suppressive role of PGD2 and its signaling axis

In examining PGD2, our analysis revealed that this mediator is predominantly synthesized by Oligo, Mast, Fibro, and pDC populations. The downstream communication network driven by this metabolite is organized into two major pathways: the PGD2 ~ SLCO2A1 axis, which chiefly enables signaling directed toward non-Lymphoid compartments, and the PGD2 ~ PTGDR axis, which primarily governs interactions among Lymphoid lineages. These relationships are illustrated in **Figure 3a.**

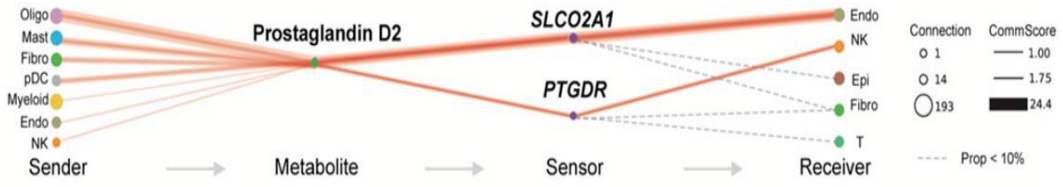

a)

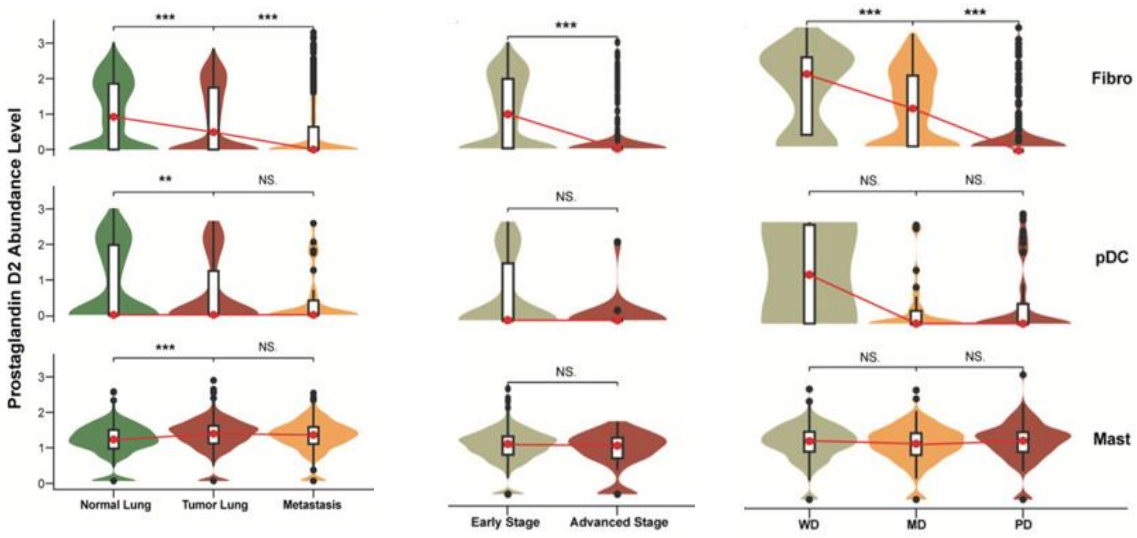

b) c) d)

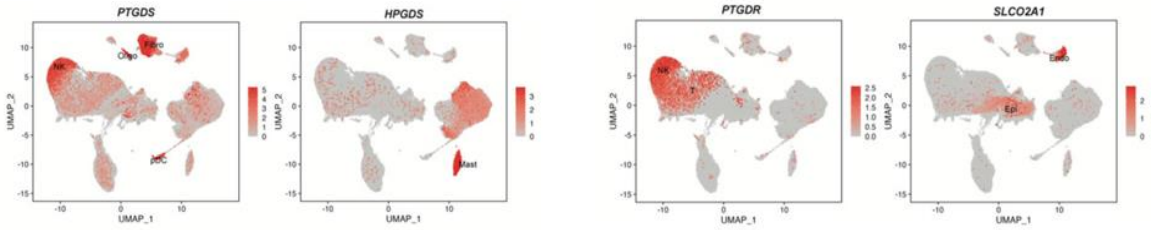

e) f)

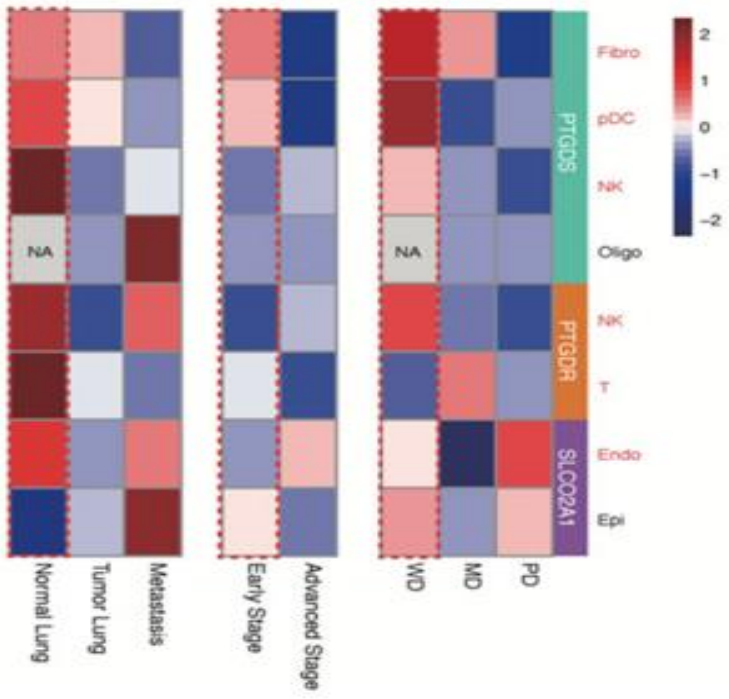

g)

Figure 3. PGD2 and its enzymes and sensor levels. (a) This panel presents a schematic illustrating how Prostaglandin D2 (PGD2) mediates signaling from sender to receiver cell populations through its two principal sensors, SLCO2A1 and PTGDR. Dot sizes correspond to the number of detected communication events, reflecting how frequently each component is used across all signaling routes. Solid red connections denote interactions with communication scores exceeding 1, with line thickness representing the magnitude of these scores, using the same scoring framework applied in **Figure 2e**. Interactions with scores below 1 are marked by dashed gray lines. (b) Violin plot illustrating the abundance of PGD2 in the three leading PGD2-producing cell types (excluding Oligo) within Tumor Lung and Normal Lung tissues. (c) Violin plot demonstrating PGD2 abundance among the same top sender cell types (again excluding Oligo), stratified by early versus advanced disease stages. (d) Violin plot mapping PGD2 levels in these sender populations (excluding Oligo) across well-, moderately-, and poorly differentiated cell states**.**
Significance was evaluated using the Wilcoxon test, with adjusted p-values annotated as *p < 0.05, **p < 0.01, ***p < 0.001, and NS for > 0.05. (e) UMAP projections colored by the expression of the PGD2-producing enzymes PTGDS and HPGDS. (f) UMAP projections highlighting the expression profiles of the PGD2 sensors PTGDR and SLCO2A1. (g) Heatmap comparing PTGDS, PTGDR, and SLCO2A1 expression across the same sample groupings depicted in (b)–(d), focusing on major sender and receiver cell categories. Colors reflect Z-score normalized mean expression.

Because Oligo cells appear only in brain metastasis samples, they are not included in subsequent analyses. Among the other dominant PGD2-abundant populations—Fibro, pDC, and Mast cells—PGD2 levels demonstrate a clear downward trajectory when comparing Normal Lung → Tumor Lung → metastatic brain tissues **(Figure 3b)**. The same decline is reproduced when stratifying by disease stage **(Figure 3c)** and by differentiation status (well, moderate, poor; **Figure 3d**).
Although Mast cells maintain comparatively elevated PGD2 levels, their trend across conditions is less pronounced.
Regarding PGD2 biosynthesis, both PTGDS and HPGDS function as the central enzymatic regulators. Our analysis shows that Mast, Fibro, pDC, and even NK/T cells rely on PTGDS, while HPGDS expression is essentially confined to Mast cells **(Figure 3e)**. For sensing pathways, PTGDR is specifically enriched in subsets of NK/T cells, whereas SLCO2A1 is preferentially expressed by Endo cells and a minor subset of Epi cells **(Figure 3f)**. As seen for PGD2 itself, expression of PTGDS, PTGDR, and SLCO2A1 also diminishes progressively across tissue types, disease stages, and differentiation states.

Taken together, these convergent patterns support the notion that PGD2 and its associated signaling machinery exert a tumor-suppressive influence in LUAD.

To reinforce these observations, integrated pan-cancer datasets containing LUAD or lung-derived samples (including normal tissues) were analyzed. Across these datasets, the spatial distributions and progression-associated behaviors of PTGDS, PTGDR, HPGDS, and SLCO2A1 closely mirrored the patterns observed in our study. This cross-cohort agreement strengthens the conclusion that PGD2-associated axes have conserved roles across distinct tumor microenvironment contexts.

Function of PGD2 signaling axis in receiver cells

To explore how the PGD2 system mediates its tumor-suppressive effects, we examined the functional properties of its sensors within receiver cells. SLCO2A1, which encodes an organic anion transporter, enables uptake of PGD2 through a lactate-exchange mechanism [36]. Genes encoding the lactate-metabolizing enzymes LDHA and LDHB are broadly expressed across cell types, including Endo cells **(Figure 4a).**

Using LDHA and LDHB expression profiles, we derived an L-lactate dehydrogenase score for Endo cells. SLCO2A1^{+} Endo cells exhibited significantly elevated scores ($p < 0.05$; **Figure 4b**). These findings suggest that the PGD2 ~ SLCO2A1 axis may contribute to lactate efflux dynamics in endothelial cells, providing a mechanistic link to its tumor-suppressive activity.

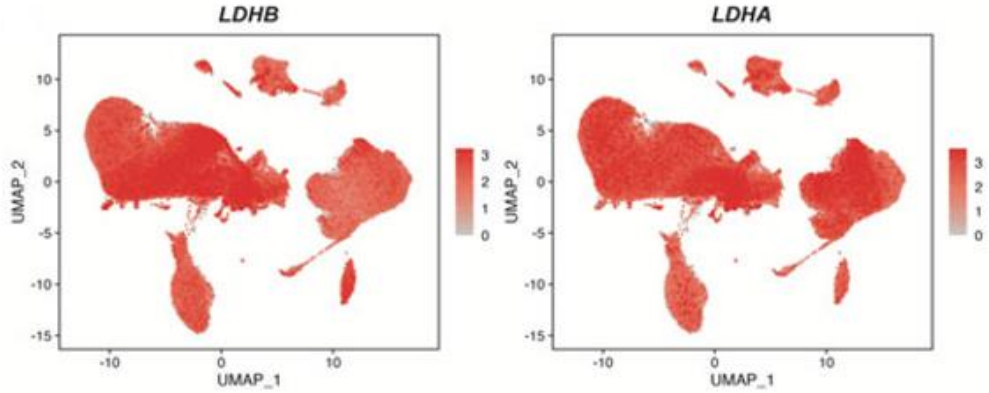

a)

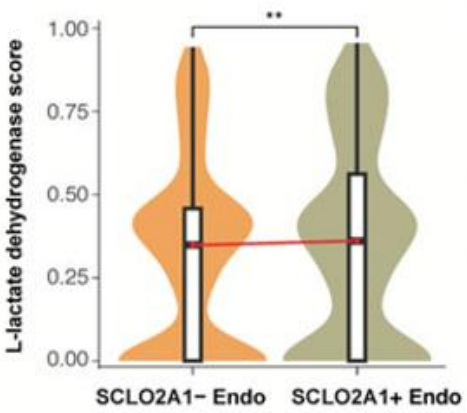

b)

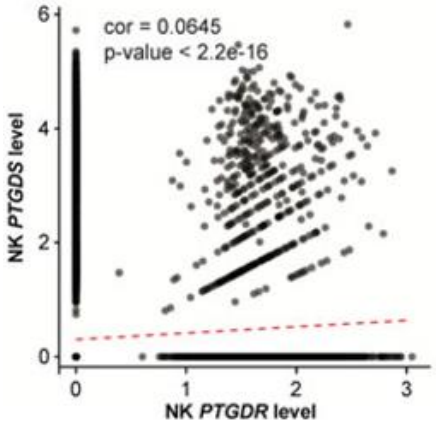

c)

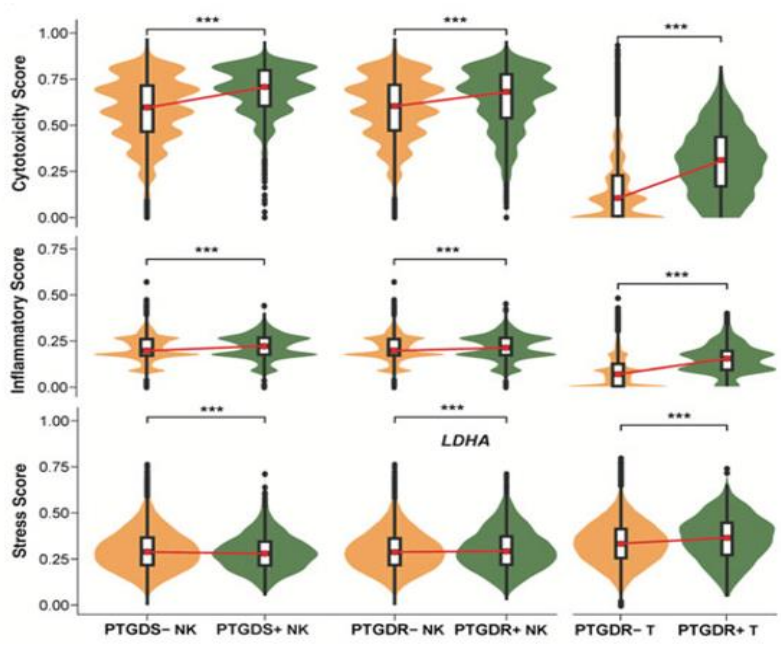

d)

Figure 4. Correlation and functional role of Prostaglandin D2 in receiver cells. (a) UMAP visualization displaying the distribution of LDHA and LDHB expression, the two genes encoding L-lactate dehydrogenase. (b) Violin plots presenting the L-lactate dehydrogenase activity score in SLCO2A1–positive and SLCO2A1–negative endothelial cells. (c) Scatter plot illustrating the relationship between PTGDS and PTGDR transcripts in NK cells (Pearson $r = 0.0645$, $p < 2.2\times10^{-16}$). (d) Violin plots showing cytotoxicity, inflammatory, and stress signatures in $PTGDS^{+/-}$ and $PTGDR^{+/-}$ NK and T cells. The functional scores in panels B and D reflect the AUCell-derived enrichment of predefined gene signatures (see Methods). Significance analyses were performed using the Wilcoxon test, with adjusted p-value categories: $*p < 0.05$, $**p < 0.01$, $***p < 0.001$, NS > 0.05.

Our analysis of NK cells revealed evidence of PGD2-mediated autocrine communication, although its magnitude appears somewhat lower than the paracrine interactions highlighted in **Figure 3a**. To explore this possibility, we examined the expression relationship between PTGDS (encoding prostaglandin-H2 D-isomerase) and PTGDR (encoding the PGD2 receptor). Their statistically significant yet modest correlation **(Figure 4c)** supports the idea that NK cells are capable of engaging in autocrine PGD2 ~ PTGDR signaling, but also suggests that paracrine PGD2 inputs likely contribute substantially to this communication axis.

We next evaluated how PGD2-related genes shape NK and T cell behavior by comparing functional signatures in PTGDS- and PTGDR-expressing subsets. $PTGDS^{+}$ NK cells, $PTGDR^{+}$ NK cells, and $PTGDR^{+}$ T cells displayed conspicuously elevated cytotoxicity and inflammatory scores, reflecting heightened immune activation and pointing toward a potential antitumor contribution from these PGD2-responsive populations **(Figure 4d)**. While these subsets also showed statistically significant differences in stress-associated signatures, their median stress levels remained relatively moderate, implying a limited effect on general cellular stress responses.

PGD2 signaling axis in NK and T cell subpopulations

To refine our understanding of which immune subsets actively participate in the PGD2 pathway, we further delineated the NK and T cell subclusters contributing to this signaling axis **(Figures 5 and 6).**

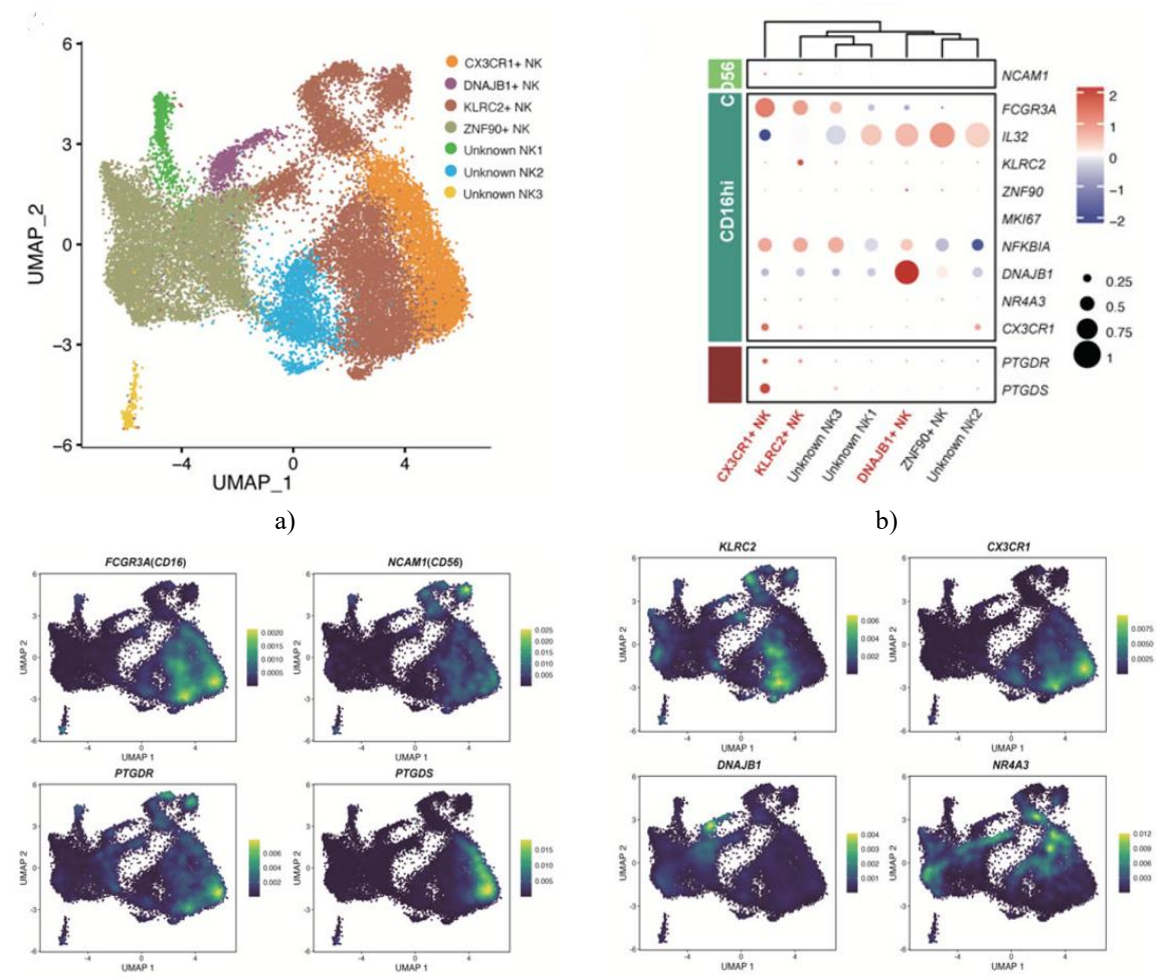

Figure 5. Enzyme gene PTGDS and receptor gene PTGDR observed in NK cells. (a) A UMAP representation of NK cells, annotated by their refined sub-cluster identities. (b) A dot chart summarizing the distribution of sub-cluster–specific marker genes. In this plot, color intensity reflects the relative expression magnitude (Z-score normalized mean values), whereas dot diameter corresponds to the proportion of cells within each sub-cluster expressing the respective marker. (c) UMAP projections illustrating the spatial expression profiles of PTGDS, PTGDR, and representative NK cell markers. (d) Additional UMAP maps visualizing the expression of KLRC2, CX3CR1, DNAJB1, and NR4A3.

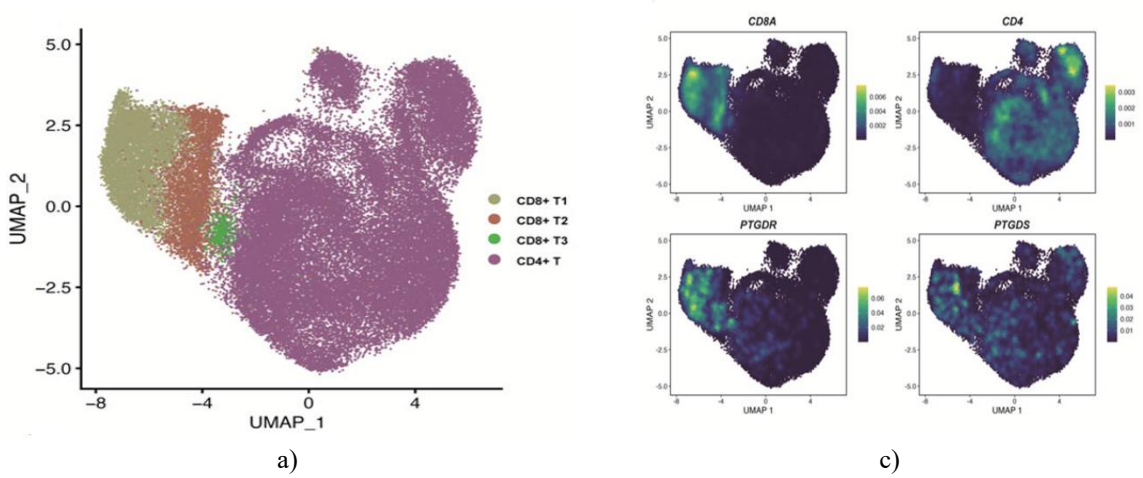

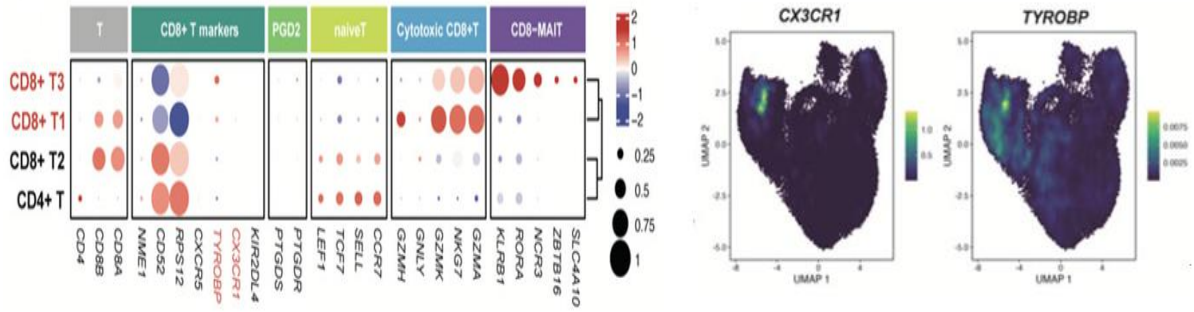

b) d)

Figure 6. Enzyme gene PTGDS and receptor gene PTGDR observed in T cells. (a) UMAP projection of T cells, annotated by refined sub-cluster identities. (b) Dot plot showing marker gene expression across sub-clusters. Dot color intensity represents Z-score normalized mean expression, while dot size indicates the fraction of cells in each sub-cluster. (c, d) UMAP maps depicting the expression levels of PTGDS, PTGDR, and canonical T cell markers.

In the NK cell compartment, six distinct subpopulations were identified **(Figure 5a)**. Previous pan-cancer analyses classified NK cells into two main populations: $CD56^{dim}CD16^{hi}$ and $CD56^{bright}CD16^{lo}$ [20]. In LUAD samples, PTGDS+ NK cells largely corresponded to the $CD56^{dim}CD16^{hi}$ population, whereas PTGDR+ NK cells were present in both NK cell populations, with a greater prevalence in $CD56^{dim}CD16^{hi}$ cells **(Figures 5b and 5c)**. These results suggest that the PGD2 signaling axis does not strongly align with the CD56/CD16 NK classification. Notably, CX3CR1+ NK cells co-expressed high levels of both PTGDS and PTGDR, hinting at a potential link between CX3CR1 expression and PGD2 autocrine signaling. Conversely, DNAJB1+ NK and KLRC2+ NK cells predominantly expressed PTGDR, indicating involvement in PGD2 paracrine signaling. A subpopulation labeled Unknown NK1, expressing IL32 and likely associated with NK-mediated inflammation, showed low-level PTGDR expression. These patterns were further validated using external datasets.

T cells were stratified into CD8+ and CD4+ lineages **(Figure 6a)** using canonical markers CD8A and CD4 **(Figures 6b and 6c).** Expression of PTGDS and PTGDR was largely restricted to CD8+ T cells, prompting further subdivision into CD8+ T1, CD8+ T2, and CD8+ T3. Both CD8+ T1 and CD8+ T3 cells showed high expression of PTGDS and PTGDR. Functionally, CD8+ T1 cells were enriched for cytotoxic markers (GZMA, GZMH, GZMK, GNLY, NKG7), whereas CD8+ T3, resembling mucosal-associated invariant T (MAIT) cells, expressed SLC4A10, ZBTB16, NCR3, RORA, and KLRB1. Both subsets exhibited strong TYROBP expression, and CD8+ T1 cells additionally expressed CX3CR1, paralleling NK cell patterns **(Figure 6d)**. These correlations were validated using an independent CD8+ T cell dataset.

Prognostic significance of the PGD2 signaling axis

To assess clinical relevance, three bulk RNA datasets (TCGA-LUAD, GSE31210, GSE37745) were analyzed. Expression of PGD2 axis genes (HPGDS, PTGDS, PTGDR, SLCO2A1) was markedly lower in tumor tissue compared to normal lung in the TCGA-LUAD cohort **(Figure 7a)**. Stage-specific differences were less pronounced. Spearman correlation analysis revealed significant positive associations between these genes and StromalScore, ImmuneScore, and ESTIMATEScore, whereas TumorPurity exhibited negative correlations across all cohorts **(Figure 7b).** These results support the notion that PGD2-mediated cell-cell communication predominantly occurs between immune and stromal cells, influencing immune infiltration levels.

Top 20 marker genes from major populations were compiled into custom gene sets, and ssGSEA scores were calculated to estimate cell-type enrichment in bulk RNA. Notably, enrichment of DNAJB1+ NK, KLRC2+ NK, and CX3CR1+ NK cells correlated strongly with PTGDR expression **(Figure 7c).** Furthermore, Hot scores were calculated for all samples, revealing that PGD2 axis genes, especially PTGDS and PTGDR, were significantly associated with both Hot scores and PD-L1 expression **(Figure 7d),** suggesting that active PGD2 signaling may enhance immunotherapy responsiveness. ROC analysis confirmed predictive performance, with AUC values ranging from 0.674–0.765 for PTGDS and 0.693–0.789 for PTGDR **(Figures 7e and 7f)**, supporting their potential as biomarkers for distinguishing immunologically "hot" versus "cold" tumors.

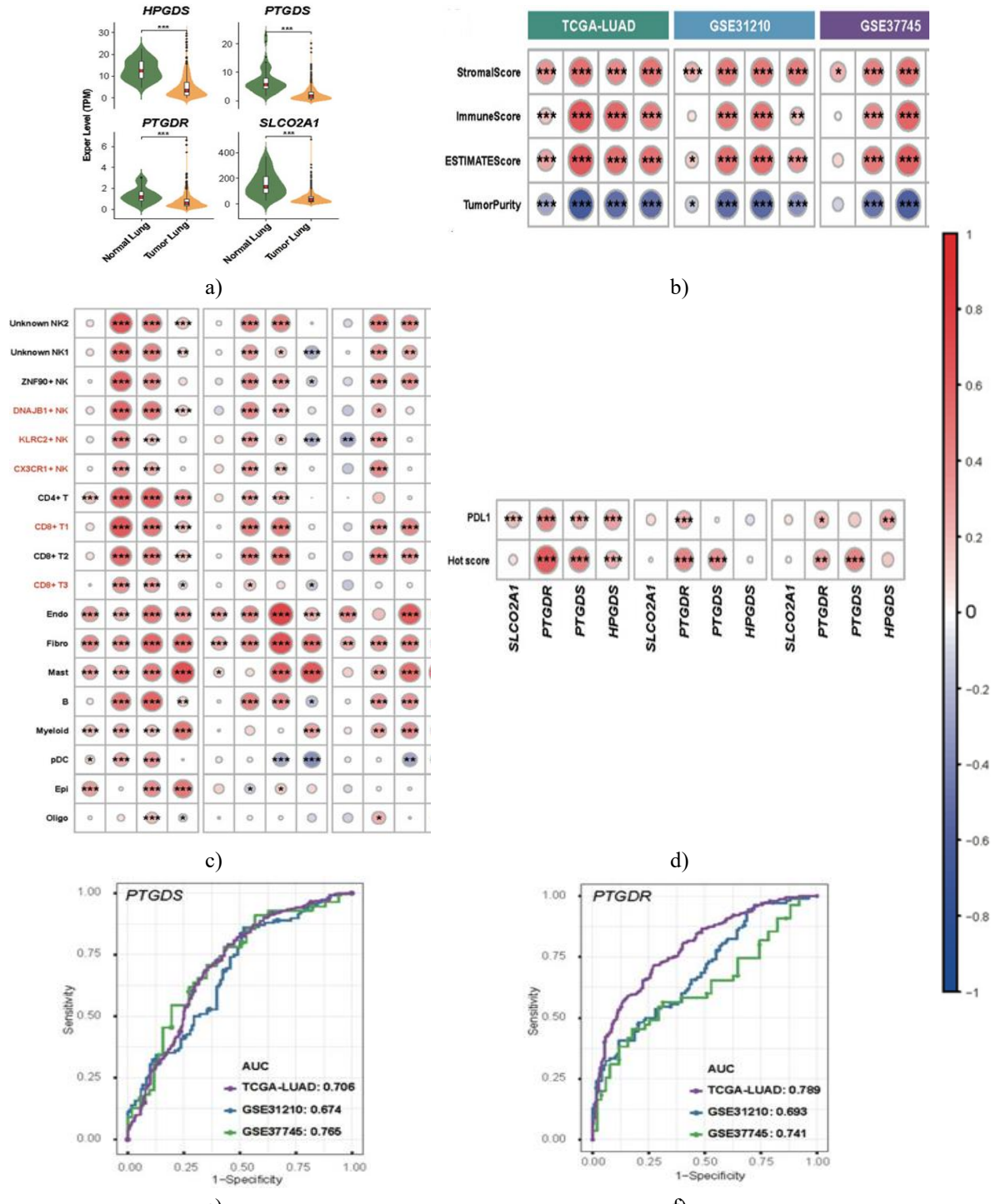

Figure 7. Expression of PGD2-associated enzyme and sensor genes in bulk RNA datasets. (a) Violin plots depicting expression levels of PGD2-related enzymes and receptors (HPGDS, PTGDS, PTGDR, SLCO2A1) in tumor versus normal lung tissues from the TCGA-LUAD cohort. Statistical significance was assessed using the Wilcoxon test: *p < 0.05, **p < 0.01, ***p < 0.001, NS > 0.05. (b) Heatmap showing Spearman correlation coefficients between these genes and StromalScore, ImmuneScore, and TumorPurity across three bulk RNA datasets. (c) Heatmap correlating PGD2 genes with cell type-specific signature scores. (d) Heatmap depicting Spearman correlations between PGD2 axis genes and PD-L1 expression as well as Hot scores. (e, f) ROC curves illustrating the ability of PTGDS (e) and PTGDR (f) to distinguish "hot" versus "cold" tumors in bulk datasets. All correlation significance levels in (b–d) are indicated by p-values: *p < 0.05, **p < 0.01, ***p < 0.001. Score calculations are detailed in Methods.

Risk model construction based on PGD2 signaling axis genes

Using the TCGA-LUAD dataset, we first applied univariate Cox regression to evaluate the prognostic impact of PGD2 axis genes (HPGDS, PTGDS, PTGDR, SLCO2A1) **(Figure 8a)**. Results indicated that PTGDS, PTGDR, and HPGDS were associated with reduced risk, with hazard ratios (HRs) of 0.9001 (95% CI: 0.8341–0.9713, $p < 0.05$), 0.7905 (95% CI: 0.6025–1.0371, $p = 0.0897$), and 0.9611 (95% CI: 0.9298–0.9934, $p < 0.05$), respectively. Next, Kaplan-Meier (KM) survival analysis was performed for each gene individually. Patients were stratified into high- and low-expression groups based on optimal cut-offs. The KM curves revealed that higher expression of PTGDS, HPGDS, and PTGDR was significantly associated with improved overall survival (OS) (log-rank $p < 0.001$ for all) **(Figure 8b)**, highlighting their potential as prognostic biomarkers.

We then built a multivariate Cox regression risk model incorporating these three genes:

Risk score=PTGDS×(−0.07927835)+PTGDR×(−0.09647698)+HPGDS×(−0.0307662)

Variance Inflation Factor (VIF) values for PTGDR, HPGDS, and PTGDS were 1.15, 1.05, and 1.20, respectively, all well below the threshold of 5, indicating minimal multicollinearity.

The risk score was independent of clinical covariates such as stage, T (tumor size), N (lymph node), M (metastasis), age, and gender **(Figure 8c)**. Patients were then stratified into high-risk and low-risk groups using the optimal cut-off. KM analysis showed that high-risk patients had significantly worse OS than low-risk patients (log-rank $p < 0.001$) **(Figure 8d)**. Median survival times were 1,194 days for high-risk versus 1,778 days for low-risk groups, supporting the predictive value of the model.

External validation using GSE31210 and GSE37745 datasets confirmed model robustness. Time-dependent ROC analysis revealed moderate predictive performance, with AUC values of 0.650 at 1 year, 0.592 at 3 years, and 0.564 at 5 years **(Figure 8e)**. Although discrimination decreased over time, the model retained reasonable prognostic capability, particularly in the early follow-up period.

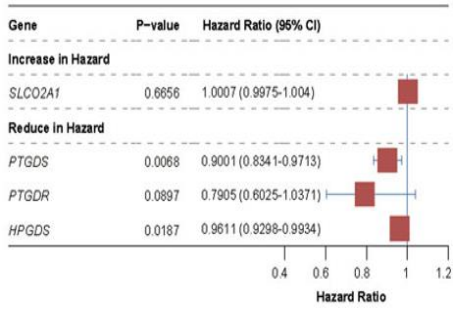

a)

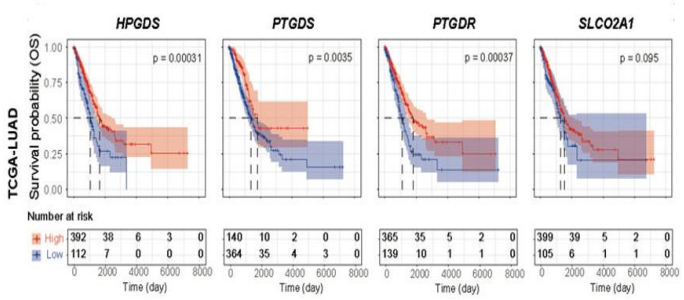

b)

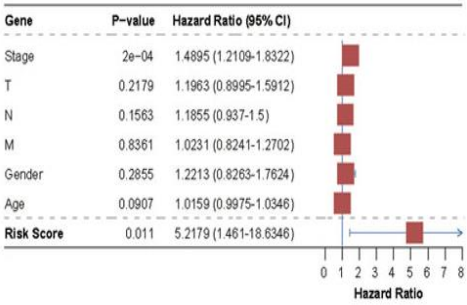

c)

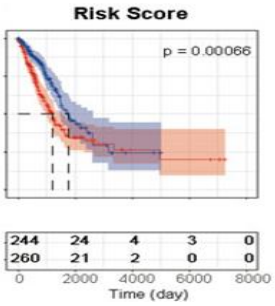

d)

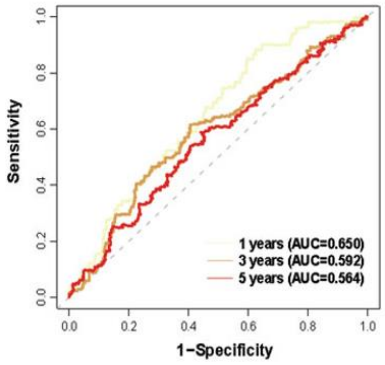

e)

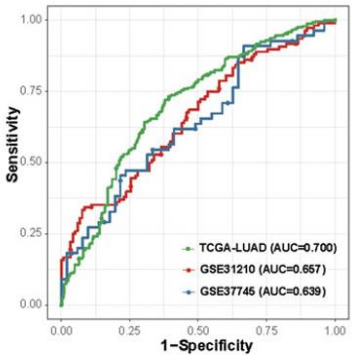

g)

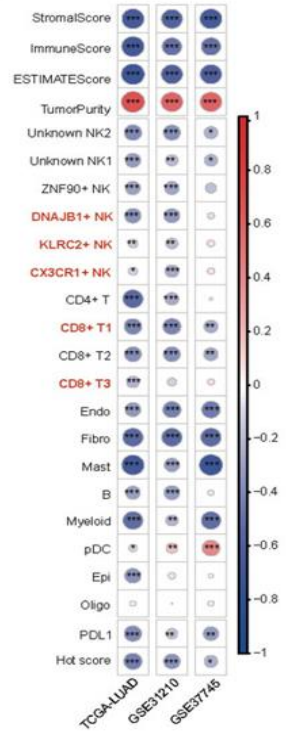

f)

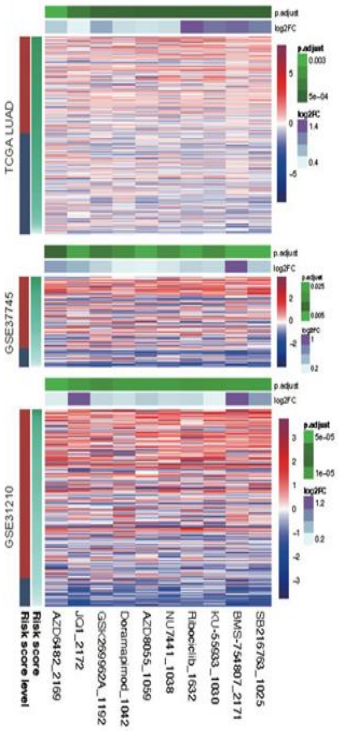

h)

Figure 8. Clinical risk assessment using PGD2 enzyme and receptor genes. (a) Forest plot depicting hazard ratios (HR) from univariate Cox proportional hazards analysis, showing associations between individual PGD2-related genes and overall survival (OS). HRs are presented with 95% confidence intervals, with statistically significant results highlighted. (B) Kaplan–Meier survival curves stratified by single-gene expression in the TCGA-LUAD cohort. (c) Multivariate Cox proportional hazards model; arrowheads indicate the limits of lines extending beyond the plot area. (d) Kaplan–Meier survival curves based on combined Cox risk score (TCGA-LUAD). (e) Time-dependent ROC curves at 1-, 3-, and 5-year follow-up

points. (f) Spearman correlation between the calculated risk score and immune-related metrics shown in **Figures 7b–7d**. (g) ROC curves evaluating the ability of the risk score to classify "hot" versus "cold" tumors; AUC values are labeled per dataset. (h) Heatmap of differential drug sensitivity predicted using the GDSC2 database (198 drugs) across three datasets, comparing high- and low-risk groups (Wilcoxon test, $p < 0.05$).

Correlation with immune landscape and tumor classification

We analyzed associations between the risk score, Hot score, and immune infiltration metrics across all cohorts **(Figure 8f)**. Spearman correlation revealed that higher risk scores were significantly associated with lower immune infiltration and higher TumorPurity, suggesting that elevated risk corresponds to a more immunologically "cold" tumor microenvironment. Consistently, ROC analysis confirmed that the risk model effectively discriminates between hot and cold tumors **(Figure 8g)**, supporting the protective role of PGD2 axis genes in promoting immune infiltration.

Drug sensitivity prediction

Using the GDSC2 dataset, we predicted IC50 values for 198 drugs in TCGA-LUAD, GSE31210, and GSE37745 cohorts. Differential analysis (Wilcoxon test, $p < 0.05$) based on high- versus low-risk groups identified ten drugs with significant sensitivity differences across all datasets: SB216763, KU-55933, NU7441, Doramapimod, AZD8055, GSK269962A, Ribociclib, AZD6482, BMS-754807, and JQ1 **(Figure 8h**). Notably, lower risk scores corresponded to decreased IC50 values, indicating higher drug sensitivity, demonstrating that this risk model can inform both prognostic stratification and potential therapeutic guidance.

Validation of PTGDS and PTGDR expression in LUAD tissues

To verify the expression patterns of PTGDS and PTGDR, we performed RT-qPCR on five paired LUAD tumor and adjacent normal lung tissues. Results showed that both genes were downregulated in tumor tissues, with PTGDS significantly reduced (*$p < 0.05$) and PTGDR showing a non-significant reduction (NS, $p > 0.05$) **(Figure 9a).**

Multiplex immunofluorescence staining further confirmed these findings at the protein level **(Figures 9b–9d)**. Both CD56+ NK cells and CD8+ T cells co-expressed PTGDR, but relative fluorescence intensity was lower in tumor tissues compared to normal tissues **(Figures 9c and 9d**; $p < 0.05$). Collectively, these results indicate that PGD2 axis genes are downregulated in LUAD, with reduced expression evident in key immune cell populations within the tumor microenvironment.

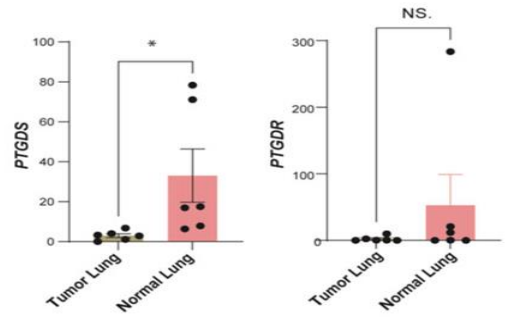

a)

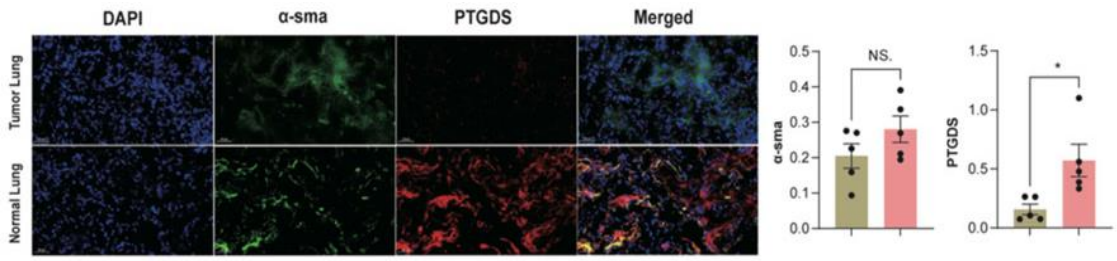

b)

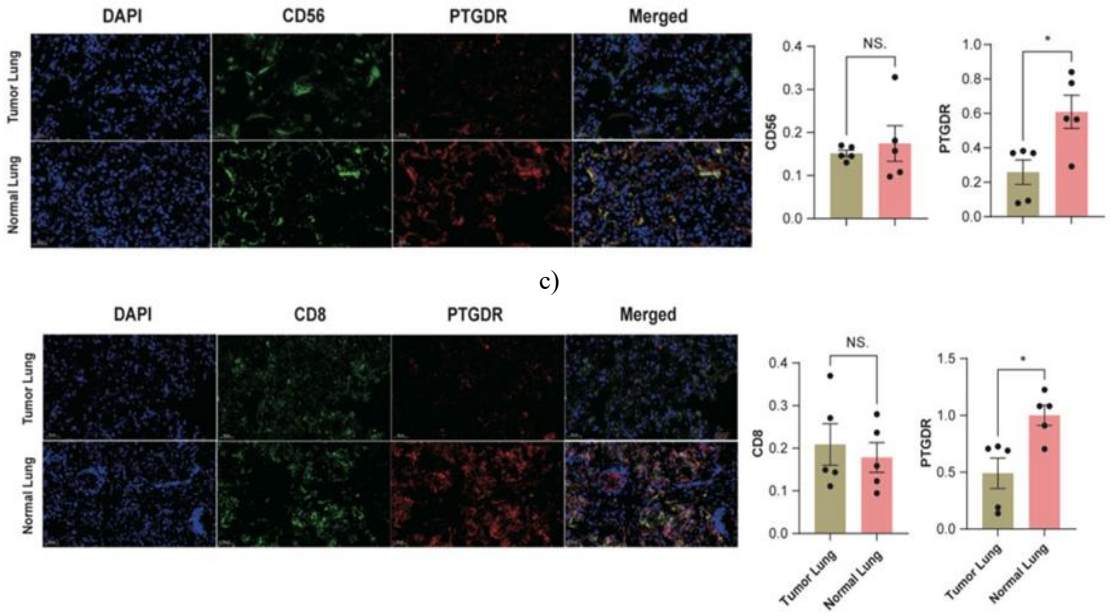

Figure 9. Experimental validation of PTGDS and PTGDR expression in LUAD and normal tissues (n = 5). (a) Relative mRNA expression levels of PTGDS and PTGDR in paired LUAD tumor and normal lung tissues. (b) Representative multiplex immunofluorescence images showing α-SMA+ PTGDS+ fibroblasts. (c) CD56+ PTGDR+ NK cells. (d) CD8+ PTGDR+ T cells.

For each panel, quantification of relative fluorescence intensity for α-SMA/PTGDS in fibroblasts, CD56/PTGDR in NK cells, and CD8/PTGDR in T cells is shown on the right. Statistical significance was determined using a two-sided t-test (*$p < 0.05$; NS > 0.05).

Tumor metabolism and its impact on the tumor microenvironment (TME) have gained increasing attention in oncology research [1-3]. Despite advances, the mechanisms by which metabolites mediate intercellular communication remain incompletely understood. Modern single-cell transcriptomic approaches provide new opportunities to investigate these processes. Leveraging these techniques, our study identifies PGD2 as a critical metabolite mediating intercellular communication in LUAD, and we systematically characterize its signaling axis, immune-modulatory roles, and therapeutic potential, offering a roadmap for future metabolite biomarker discovery.

Prostaglandins (PGs) are widely recognized modulators of cancer biology, with PGE2 often acting as a prototypical tumor-promoting factor [37]. In contrast, PGD2 exhibits tumor-suppressive properties, with PTGDS/PGD2 functioning in a tissue-specific manner across multiple cancers [38-42]. However, most existing studies rely heavily on in vitro experiments, leaving its mechanisms and intercellular effects in the TME underexplored [39, 43, 44]. Prior work has largely focused on the PGD2/PTGDR2 receptor-ligand axis [45]. Early evidence in lung cancer suggested PGD2's tumor-suppressive role [46], with mast cell-derived PGD2 modulating vascular permeability and TNF-α production to regulate the TME [42]. L-PGDS expression has been observed to decrease during tumor progression [47], and exogenous L-PGDS can inhibit proliferation and PDGF-induced migration of A549 cells. Despite these findings, the in vivo production of PGD2 and its effects on immune cells in LUAD remain largely unclear.

Our study demonstrates that PGD2 is predominantly produced by PTGDS-expressing fibroblasts, mast cells, and pDCs, and signals to NK and T cells via the PTGDR receptor and to endothelial cells via the SLCO2A1 transporter. Expression analysis in paired LUAD tissues confirmed downregulation of PTGDS in fibroblasts and PTGDR in NK/T cells at both mRNA and protein levels. These findings highlight PGD2 as a metabolic signaling hub linking tumor metabolism to immune modulation in LUAD.

Regarding PGD2-producing cells, mast cells are the primary source via HPGDS, consistent with prior studies [42]. Additional contributors include fibroblasts, pDCs, and certain NK/T cell subsets. Interestingly, oligodendrocytes produce PGD2 in brain metastases. For receptor-expressing cells, we propose that CX3CR1+ NK/T cells utilize the PGD2~PTGDR autocrine pathway to enhance cytotoxicity and antitumor effects.

Meanwhile, KLRC2+ NK cells, DNAJB1+ NK cells, and CD8+ MAIT cells appear to participate in PGD2 paracrine signaling. Although PGD2 may facilitate lactate efflux through SLCO2A1 on endothelial cells, this hypothesis requires further experimental validation. Collectively, these findings expand current knowledge of PGD2 signaling in LUAD.

Previous research underscores PGD2's role in immune regulation [48]. We reveal that CX3CR1+ NK/T cells specifically engage in the PGD2~PTGDR autocrine loop. CX3CR1, the receptor for CX3CL1 (fractalkine), is expressed on CD8+ T cells and NK cells [49]. While CX3CL1:CX3CR1 signaling in myeloid cells may promote tumor growth and migration [50, 51], its bulk-level expression serves as a positive prognostic marker in LUAD [52]. Our findings suggest that CX3CR1+ NK/T cells, through the PGD2 autocrine axis, maintain high cytotoxic and immune activity, highlighting PGD2's nuanced and context-dependent role in shaping antitumor immunity.

We observed that several receptor cell types—KLRC2+ NK cells, DNAJB1+ NK cells, and CD8+ MAIT cells—participate in PGD2-driven paracrine signaling. Literature suggests that these populations possess antitumor capabilities within the tumor microenvironment. KLRC2+ NK cells, often described as adaptive NK cells, exhibit reduced cytotoxic activity against autologous or activated immune cells [53]. DNAJB1+ NK cells are characterized by high cellular stress scores [20], and CD8+ MAIT cells are multifunctional, capable of both promoting inflammatory responses and mediating antitumor effects [54]. Collectively, these receptor populations seem to have a less pronounced tumor-killing capacity compared with CX3CR1+ NK/T cells, reflecting more nuanced regulatory roles. This is supported by our data, where cytotoxicity-related gene expression in CD8+ T1 (CD8+ MAIT cells) was substantially lower than in CD8+ T1 (CX3CR1+ T cells). This indicates that the intrinsic ability of CX3CR1+ NK/T cells to secrete PGD2 correlates strongly with their cytotoxic potency. Interestingly, some NK/T cells that do not produce PGD2 still express the PTGDR receptor, suggesting that paracrine PGD2 from neighboring cells or exogenous sources may enhance their antitumor functions in vivo.

The relevance of PGD2 signaling in LUAD was further corroborated through bulk RNA-seq datasets, supporting the broader applicability of our findings. Consistent gene expression patterns across independent cohorts suggest that the PGD2 axis could serve as a biomarker for immune activity and might be leveraged for both prognostic assessment and therapy monitoring. Considering that immune checkpoint therapies have limited success in specific LUAD subsets, interventions targeting PGD2 signaling could represent an alternative or adjunct approach to bolster antitumor immunity.

Our study has limitations that should be acknowledged. First, metabolite abundance was inferred from single-cell transcriptomic data, which may not fully capture metabolic dynamics; future validation with direct metabolomics would be valuable. Second, the proposed link between PGD2 signaling and lactate efflux requires additional experimental verification. Third, the predictive performance of our PGD2-based risk model varied across validation cohorts, likely influenced by batch effects in bulk RNA data.

Conclusion

In conclusion, PGD2 emerges as a pivotal metabolite within the LUAD tumor microenvironment, orchestrating communication through the PGD2~SLCO2A1 and PGD2~PTGDR signaling axes. Our findings indicate that PGD2 exerts tumor-suppressive effects predominantly by activating NK and T cells, highlighting its role in regulating antitumor immune responses. These results demonstrate the significance of PGD2 in coordinating metabolic and immune networks in LUAD, emphasizing its potential as both a prognostic biomarker and a therapeutic target. Overall, the PGD2 axis contributes to tumor suppression and immune modulation, offering promising avenues for improving patient prognosis and guiding treatment strategies.

Acknowledgments: None

Conflict of Interest: Authors YM, BZ, and FL were employed by Hangzhou Astrocyte Technology Co., Ltd. The remaining authors declare that the research was conducted in the absence of any commercial or financial relationships that could be construed as a potential conflict of interest.

Financial Support: The author(s) declare that financial support was received for the research and/or publication of this article. This work was financially supported by the projects of Young Scientists Fund of the National Natural Science Foundation of China (62203117) and the Huadong Hospital Clinical Trail Foundation, China (HDLC2022012).

Ethics Statement: The studies involving humans were approved by the Ethics Committee of the Fuyang People's Hospital. The studies were conducted in accordance with the local legislation and institutional requirements. The participants provided their written informed consent to participate in this study. The manuscript presents research on animals that do not require ethical approval for their study.

References

1. Mao Y, Xia Z, Xia W, Jiang P. Metabolic reprogramming, sensing, and cancer therapy. Cell Rep. 2024;43(5):115064. doi:10.1016/j.celrep.2024.115064
2. Nong S, Han X, Xiang Y, Qian Y, Wei Y, Zhang T, et al. Metabolic reprogramming in cancer: mechanisms and therapeutics. MedComm. 2023;4(1):e218. doi:10.1002/mco2.218
3. Park JH, Pyun WY, Park HW. Cancer metabolism: phenotype, signaling and therapeutic targets. Cells. 2020;9(10):2308. doi:10.3390/cells9102308
4. Wang YP, Lei QY. Metabolite sensing and signaling in cell metabolism. Signal Transduct Target Ther. 2018;3(1):30. doi:10.1038/s41392-018-0024-7
5. Liu S, Alexander RK, Lee CH. Lipid metabolites as metabolic messengers in inter-organ communication. Trends Endocrinol Metab. 2014;25(7):356-63. doi:10.1016/j.tem.2014.05.002
6. Zhu Y, Fang S, Fan B, Xu K, Xu L, Wang L, et al. Cancer-associated fibroblasts reprogram cysteine metabolism to increase tumor resistance to ferroptosis in pancreatic cancer. Theranostics. 2024;14(7):1683-700. doi:10.7150/thno.8980
7. Alghamdi NCW, Dang P, Lu X, Wan C, Gampala S, Huang Z, et al. A graph neural network model to estimate cell-wise metabolic flux using single cell RNA-seq data. Genome Res. 2021;31(10):1867-84. doi:10.1101/gr.271205.120
8. Nathaniel J, Liu J, Gentine P. MetaFlux: meta-learning global carbon fluxes from sparse spatiotemporal observations. Sci Data. 2023;10(1):440. doi:10.1038/s41597-023-02349-y
9. Wagner A, Wang C, Fessler J, Detomaso D, Avila-Pacheco J, Kaminski J, et al. Metabolic modeling of single Th17 cells reveals regulators of autoimmunity. Cell. 2021;184(18):4168-85.e21. doi:10.1016/j.cell.2021.05.045
10. Zheng R, Zhang Y, Tsuji T, Gao X, Wagner A, Yosef N, et al. MEBOCOST: metabolic cell-cell communication modeling by single cell transcriptome. BioRxiv. 2022. doi:10.1101/2022.01.11.475692
11. Bray F, Laversanne M, Sung H, Ferlay J, Siegel RL, Soerjomataram I, et al. Global cancer statistics 2022: GLOBOCAN estimates of incidence and mortality worldwide for 36 cancers in 185 countries. CA Cancer J Clin. 2024;74(3):229-63. doi:10.3322/caac.21834
12. Chen Z, Fillmore CM, Hammerman PS, Kim CF, Wong KK. Non-small-cell lung cancers: a heterogeneous set of diseases. Nat Rev Cancer. 2014;14(8):535-46. doi:10.1038/nrc3775
13. Klupczynska-Gabryszak A, Daskalaki E, Wheelock CE, Kasprzyk M, Dyszkiewicz W, Grabicki M, et al. Metabolomics-based search for lung cancer markers among patients with different smoking status. Sci Rep. 2024;14(1):15444. doi:10.1038/s41598-024-65835-2
14. Moreno P, Jimenez-Jimenez C, Garrido-Rodriguez M, Calderon-Santiago M, Molina S, Lara-Chica M, et al. Metabolomic profiling of human lung tumor tissues - nucleotide metabolism as a candidate for therapeutic interventions and biomarkers. Mol Oncol. 2018;12(11):1778-96. doi:10.1002/1878-0261.12369
15. Zhao C, Han S, Li X, Wu T, Zhou J, Guo Y, et al. Analysis of differential metabolites in lung cancer patients based on metabolomics and bioinformatics. Future Oncol. 2020;16(5):1269-87. doi:10.2217/fon-2019-0818
16. Nie M, Yao K, Zhu X, Chen N, Xiao N, Wang Y, et al. Evolutionary metabolic landscape from preneoplasia to invasive lung adenocarcinoma. Nat Commun. 2021;12(1):6479. doi:10.1038/s41467-021-26685-y
17. Madama D, Martins R, Pires AS, Botelho MF, Alves MG, Abrantes AM, et al. Metabolomic profiling in lung cancer: a systematic review. Metabolites. 2021;11(9):630. doi:10.3390/metabo11090630
18. Kim N, Kim HK, Lee K, Hong Y, Cho JH, Choi JW, et al. Single-cell RNA sequencing demonstrates the molecular and cellular reprogramming of metastatic lung adenocarcinoma. Nat Commun. 2020;11(1):2285. doi:10.1038/s41467-020-16164-1
19. Hao Y, Stuart T, Kowalski MH, Choudhary S, Hoffman P, Hartman A, et al. Dictionary learning for integrative, multimodal and scalable single-cell analysis. Nat Biotechnol. 2024;42(2):293-304. doi:10.1038/s41587-023-01767-y

20. Tang F, Li J, Qi L, Liu D, Bo Y, Qin S, et al. A pan-cancer single-cell panorama of human natural killer cells. Cell. 2023;186(22):4235-51.e20. doi:10.1016/j.cell.2023.07.034
21. Zheng L, Qin S, Si W, Wang A, Xing B, Gao R, et al. Pan-cancer single-cell landscape of tumor-infiltrating T cells. Science. 2021;374(6568):abe6474. doi:10.1126/science.abe6474
22. Alquicira-Hernandez J, Powell JE. Nebulosa recovers single-cell gene expression signals by kernel density estimation. Bioinformatics. 2021;37(8):2485-7. doi:10.1093/bioinformatics/btab003
23. Gao Y, Li J, Cheng W, Diao T, Liu H, Bo Y, et al. Cross-tissue human fibroblast atlas reveals myofibroblast subtypes with distinct roles in immune modulation. Cancer Cell. 2024;42(9):1764-83.e10. doi:10.1016/j.ccell.2024.08.020
24. Cheng S, Li Z, Gao R, Xing B, Gao Y, Yang Y, et al. A pan-cancer single-cell transcriptional atlas of tumor infiltrating myeloid cells. Cell. 2021;184(5):792-809.e23. doi:10.1016/j.cell.2021.01.010
25. Foy JP, Karabajakian A, Ortiz-Cuaran S, Boussageon M, Michon L, Bouaoud J, et al. Immunologically active phenotype by gene expression profiling is associated with clinical benefit from PD-1/PD-L1 inhibitors in real-world head and neck and lung cancer patients. Eur J Cancer. 2022;174:287-98. doi:10.1016/j.ejca.2022.06.034
26. Aibar S, Gonzalez-Blas CB, Moerman T, Huynh-Thu VA, Imrichova H, Hulselmans G, et al. SCENIC: single-cell regulatory network inference and clustering. Nat Methods. 2017;14(11):1083-6. doi:10.1038/nmeth.4463
27. Subramanian A, Mootha VK, Mukherjee S, Ebert BL, Gillette MA, Paulovich A, et al. Gene set enrichment analysis: a knowledge-based approach for interpreting genome-wide expression profiles. Proc Natl Acad Sci U S A. 2005;102(43):15545-50. doi:10.1073/pnas.0506580102
28. Therneau T. A package for survival analysis in R. 2024.
29. Sthda AK. Survminer R package: survival data analysis and visualization; 2016.
30. Patrick J, Heagerty PS-C. Compute time-dependent ROC curve from censored survival data using Kaplan-Meier (KM) or nearest neighbor estimation (NNE) method of Heagerty, Lumley and Pepe. Biometrics. 2000;56(4):1155-66.
31. Maeser D, Gruener RF, Huang RS. oncoPredict: an R package for predicting in vivo or cancer patient drug response and biomarkers from cell line screening data. Brief Bioinform. 2021;22(5):bbab260. doi:10.1093/bib/bbab260
32. Korsunsky I, Millard N, Fan J, Slowikowski K, Zhang F, Wei K, et al. Fast, sensitive and accurate integration of single-cell data with Harmony. Nat Methods. 2019;16(12):1289-96. doi:10.1038/s41592-019-0619-0
33. Song W, Wu X, Su M, Hu R, Zhao Y. The role of cholesterol metabolism and its regulation in tumor development. World J Surg Surg Res. 2024;7:1538.
34. Hua W, Ten Dijke P, Kostidis S, Giera M, Hornsveld M. TGFβ-induced metabolic reprogramming during epithelial-to-mesenchymal transition in cancer. Cell Mol Life Sci. 2020;77(10):2103-23. doi:10.1007/s00018-019-03398-6
35. Fan Y, Tan X, Zhao H, Tu X, Liu X, Wang Y. Cysteine metabolism in tumor redox homeostasis. Curr Med Chem. 2023;30(12):1813-23. doi:10.2174/0929867329666220817141227
36. Lu R, Kanai N, Bao Y, Schuster VL. Cloning, in vitro expression, and tissue distribution of a human prostaglandin transporter cDNA (hPGT). J Clin Invest. 1996;98(5):1142-9. doi:10.1172/JCI118897
37. Santiso A, Heinemann A, Kargl J. Prostaglandin E2 in the tumor microenvironment, a convoluted affair mediated by EP receptors 2 and 4. Pharmacol Rev. 2024;76(2):388-413. doi:10.1124/pharmrev.123.000901
38. Pan J, Zhang L, Huang J. Prostaglandin D2 synthase/prostaglandin D2/TWIST2 signaling inhibits breast cancer proliferation. Anticancer Drugs. 2021;32(7):1029-37. doi:10.1097/CAD.0000000000001111
39. Zhang Q, Wang F, Huang Y, Gao P, Wang N, Tian H, et al. PGD2/PTGDR2 signal affects the viability, invasion, apoptosis, and stemness of gastric cancer stem cells and prevents the progression of gastric cancer. Comb Chem High Throughput Screen. 2024;27(9):933-46. doi:10.2174/1386207326666230731103112
40. Shyu RY, Wu CC, Wang CH, Tsai TC, Wang LK, Chen ML, et al. H-rev107 regulates prostaglandin D2 synthase-mediated suppression of cellular invasion in testicular cancer cells. J Biomed Sci. 2013;20(1):30. doi:10.1186/1423-0127-20-30
41. Wu CC, Shyu RY, Wang CH, Tsai TC, Wang LK, Chen ML, et al. Involvement of the prostaglandin D2 signal pathway in retinoid-inducible gene 1 (RIG1)-mediated suppression of cell invasion in testis cancer cells. Biochim Biophys Acta. 2012;1823(11):2227-36. doi:10.1016/j.bbamcr.2012.08.013

42. Murata T, Aritake K, Matsumoto S, Kamauchi S, Nakagawa T, Hori M, et al. Prostaglandin D2 is a mast cell-derived antiangiogenic factor in lung carcinoma. Proc Natl Acad Sci U S A. 2011;108(48):19802-7. doi:10.1073/pnas.1110011108
43. Iwanaga K, Nakamura T, Maeda S, Aritake K, Hori M, Urade Y, et al. Mast cell-derived prostaglandin D2 inhibits colitis and colitis-associated colon cancer in mice. Cancer Res. 2014;74(11):3011-9. doi:10.1158/0008-5472.CAN-13-2792
44. Omori K, Morikawa T, Kunita A, Nakamura T, Aritake K, Urade Y, et al. Lipocalin-type prostaglandin D synthase-derived PGD2 attenuates malignant properties of tumor endothelial cells. J Pathol. 2018;244(1):84-96. doi:10.1002/path.4993
45. Tian H, Ge K, Wang L, Gao P, Chen A, Wang F, et al. Advances in PGD2/PTGDR2 signaling pathway in tumors: a review. Biomol Biomed. 2024;24(10):1055-67. doi:10.17305/bb.2024.10485
46. Mclemore TL, Hubbard WC, Litterst CL, Liu MC, Miller S, Mcmahon NA, et al. Profiles of prostaglandin biosynthesis in normal lung and tumor tissue from lung cancer patients. Cancer Res. 1988;48(12):3140-7.
47. Ragolia L, Palaia T, Hall CE, Klein J, Buyuk A. Diminished lipocalin-type prostaglandin D2 synthase expression in human lung tumors. Lung Cancer. 2010;70(1):103-9. doi:10.1016/j.lungcan.2010.01.011
48. Joo M, Sadikot RT. PGD synthase and PGD2 in immune response. Mediators Inflamm. 2012;2012:503128. doi:10.1155/2012/503128
49. Lysaght MJCAJ. CX3CL1 signaling in the tumor microenvironment. In: Tumor Microenvironment. Springer; 2020.
50. Okuma A, Hanyu A, Watanabe S, Hara E. p16(Ink4a) and p21(Cip1/Waf1) promote tumor growth by enhancing myeloid-derived suppressor cells chemotaxis. Nat Commun. 2017;8(1):2050. doi:10.1038/s41467-017-02281-x
51. Schmall A, AL-Tamari HM, Herold S, Kampschulte M, Weigert A, Wietelmann A, et al. Macrophage and cancer cell cross-talk via CCR2 and CX3CR1 is a fundamental mechanism driving lung cancer. Am J Respir Crit Care Med. 2015;191(4):437-47. doi:10.1164/rccm.201406-1137OC
52. Liu J, Li Y, Zhu X, Li Q, Liang X, Xie J, et al. Increased CX3CL1 mRNA expression level is a positive prognostic factor in patients with lung adenocarcinoma. Oncol Lett. 2019;17(6):4877-90. doi:10.3892/ol.2019.10211
53. Schlums H, Cichocki F, Tesi B, Theorell J, Beziat V, Holmes TD, et al. Cytomegalovirus infection drives adaptive epigenetic diversification of NK cells with altered signaling and effector function. Immunity. 2015;42(3):443-56. doi:10.1016/j.immuni.2015.02.008
54. Yigit M, Basoglu OF, Unutmaz D. Mucosal-associated invariant T cells in cancer: dual roles, complex interactions and therapeutic potential. Front Immunol. 2024;15:1369236. doi:10.3389/fimmu.2024.1369236